communications medicine

A Nature Portfolio journal

Article

https://doi.org/10.1038/s43856-026-01581-y

AI-based autism identification from hyperspectral imaging detection of oxidative stress in pediatric red blood cells

Check for updates

Roupen Vartian[1,12], Anna Sansone[1,12], Gessica Batani[1], Antonia Parmeggiani[2,4], Enzo Grossi[3], Marina Marini[4], Vincenzo Davide Catania[5], Mario Lima[5], Alessandro Ghezzo[6], Cristina Panisi[7], Marida Angotti[2], Provvidenza M. Abruzzo[4], Carmela Serpe[4], Arianna Vignini[8], Ellas Spyratou[9], Efstathios P. Efstathoupoulos[9], Chryssostomos Chatgilialoglu[1,10] & Carla Ferreri[1,11]

Abstract

Background Oxidative stress (OS) plays a key role in many pathologies, yet the non-invasive, label-free, and cost-effective detection remains a challenge. This study evaluates Hyperspectral Imaging (HSI) combined with AI to detect OS by identifying changes in red blood cell (RBC) membranes.

Methods An OS model for the HSI procedure is established by treating EDTA-anticoagulated whole blood with 1.5% hydrogen peroxide (H_2O_2) to induce stress without cell lysis. Membrane fatty acid composition (lipidome) is analysed via gas chromatography, while HSI in dark-field microscopy captures spectral signatures and their distributions in healthy and insulted RBC. The HSI methodology is then applied to RBC samples from 31 neurotypical (NT) children and 27 children with Autism Spectrum Disorder (ASD), a condition linked to OS. A deep learning algorithm is used to classify the clinical samples based on the identified OS signatures.

Results Here, we show that significant spectral distribution differences are present in OS-exposed RBCs, which correlate with membrane lipidome remodelling. Notably, the OS-induced spectral differences in the H_2O_2 model mirror those observed between the ASD and NT groups. The AI-assisted analysis successfully classifies the pediatric cohort, achieving 93.2% accuracy in identifying ASD subjects.

Conclusions HSI, guided by OS-specific modeling and integrated with AI, provides a robust, scalable method for membrane diagnostics. This approach offers a promising pathway for personalized medicine and the non-invasive monitoring of oxidative stress-related conditions.

Plain Language Summary

Oxidative stress (OS) is an imbalance that occurs in some cells within the body. It is linked to various diseases, yet it remains challenging to detect early. Methods based on hyperspectral imaging (HSI), a technique that captures imaging data beyond the human visual spectrum, offers a cost-effective, non-invasive, and precise measurement of damage to cells occurring as a result of oxidative stress. We used HSI on a single drop of blood to examine red blood cell membranes. We found that cells exposed to OS could be distinguished from healthy cells using HSI. We used this method on blood samples from children with and without Autism Spectrum Disorder (ASD). Children with ASD could be identified with over 93% accuracy through AI analysis. This AI-aided HSI approach represents a promising clinical tool that could enable earlier intervention before cellular damage leads to severe health conditions.

Oxidative stress (OS) profoundly impacts red blood cell (RBC) lifespan and function, with polyunsaturated fatty acids (PUFAs) of membrane phospholipids being primary targets of this process[1–3]. OS is involved in a broad spectrum of pathologies[4–7], highlighting the critical need for robust diagnostic and prognostic tools. The OS-related changes of the RBC membrane lipidome and its fatty acid composition result in risk factors for cardiovascular and other OS-related diseases in population studies[4–10]. At the same time, the Peroxidation Index (PI) offers valuable insights into the OS impact on aging, indicating cell membranes as a valuable target for investigation of stress exposure during life span[11–13]. Considering the whole scenario of OS-

[1]ISOF, Consiglio Nazionale delle Ricerche, Bologna, Italy. [2]IRCCS Istituto delle Scienze Neurologiche di Bologna, UOC Neuropsichiatria dell'Età Pediatrica, Bologna, Italy. [3]Fondazione Villa S. Maria, Tavernerio, CO, Italy. [4]Dipartimento di Scienze Mediche e Chirurgiche (DIMEC), University of Bologna, Bologna, Italy. [5]Pediatric Surgery Department, IRCCS Azienda Ospedaliero-Universitaria di Bologna, Bologna, Italy. [6]Fondazione Danelli ONLUS, Lodi, Italy. [7]Child Psychopathology Unit, Scientific Institute, IRCCS E. Medea, Lecco, Bosisio Parini, Italy. [8]Department of Clinical Sciences, Polytechnic University of Marche, Ancona, Italy. [9]Department of Applied Medical Physics, Medical School, National and Kapodistrian University of Athens, Athens, Greece. [10]Center of Advanced Technologies, Adam Mickiewicz University, Poznań, Poland. [11]Lipidomic Laboratory Lipinutragen, c/o Area di Ricerca Bologna, Bologna, Italy. [12]These authors contributed equally: Roupen Vartian, Anna Sansone. e-mail: carla.ferreri@cnr.it

related transformations in a living organism, a recent review has affirmed the importance of using a panel of biomarkers, rather than a single indicator, to ensure accurate and comprehensive evaluations of OS levels[3]. Beyond the challenges of detecting subtle, early signs of oxidative stress due to methodological limitations, cost constraints also present a significant hurdle.

Hyperspectral imaging (HSI) is an advanced imaging technique that combines the principles of spectroscopy with traditional imaging. Unlike conventional cameras, hyperspectral cameras capture detailed spectral information across hundreds of narrow, contiguous spectral bands of the electromagnetic spectrum for each pixel. By analyzing the light reflected or emitted by a specimen, hyperspectral imaging (HSI) can reveal necessary information about its material composition and chemical properties, but also enables the detection of geometrical and organizational features of the sample, not visible in other imaging methodologies[14,15].

Hyperspectral imaging (HSI) was initially developed for remote sensing applications, particularly on Earth-observing satellites, where it was used to monitor geological activity, assess environmental conditions, and support military surveillance. Over time, HSI has expanded into various fields, including agriculture, environmental monitoring, biomedical imaging, and molecular biology. In particular, when imaging biological specimens that interact with light, HSI captures a detailed spectral signature or "spectral fingerprint" for each pixel in the image. These signatures typically span wavelengths from the visible to near-infrared (VNIR) and short-wave infrared (SWIR) regions of the electromagnetic spectrum[16,17]. For hyperspectral imaging, a three-dimensional (3D) hyperspectral datacube is created for each pixel, with two spatial dimensions, similar to those in a regular photograph, and the third dimension containing the spectral information for each pixel (Supplementary Fig. 1a, b)[15–17]. The Spectral Angle Mapper (SAM) is a widely used algorithm for spectral classification in hyperspectral imaging. It operates through a complex mathematical process in which the spectral signature of each pixel is treated as a vector in a high-dimensional space, with each dimension corresponding to a specific spectral band. SAM then calculates the angle between these spectral vectors to assess their similarity—smaller angles indicate greater similarity. Typically, if the angle between two spectra is less than 0.10 radians, they are considered a match or classified as the same. When accompanied by SAM, HSI can identify materials by their unique spectral signature, differentiating between substances that might appear the same to the naked eye, thus detecting differences or anomalies introduced in the original sample that would otherwise be invisible. In the case of a biological specimen, such as blood, HSI allowed to distinguish blood cell morphology (for example, leukocytes from erythrocytes), to automate erythrocyte count, and also to get spectral fingerprints of molecular components, such as hemoglobin in the different redox states, the membrane lipid cluster (phospholipids, cholesterol, fatty acids), and proteins (spectrin, ankyrin, actin, protein 4.1, and protein 4.2)[18–21]. Using hyperspectral dark field microscopy (HDFM) the healthy RBC membrane scattering properties were first reported, obtaining a spectral signature, made of eight graphs, showing light intensity versus wavelength in the range 400–1000 nm; a simple statistical treatment of such spectral features combined with clinical status afforded initial insights of the power of this methodology to examine health conditions[22]. When the architecture of the RBC membrane is considered, any lipid alteration, as well as degradation or aggregation of proteins, not destructive for the cell survival, causes a rearrangement in the membrane bilayer organization, changing its refractive index, anisotropy, or geometry. It can be inferred that light scattering from the cell membrane serves as a signature of the specific cell type or status, and provides comprehensive information about changes resulting from the specific insult[23–25].

Building on advances in HSI-based biological measurements and the relevance of OS as a molecular basis of cellular changes, we develop the first HSI-based methodology for direct monitoring changes in RBC due to OS. Here, we show the use of HSI for mapping RBC membranes before and after a non-destructive oxidative insult induced by H_2O_2, a well-characterized biologically related oxidant[26–30]. Moreover, we integrate lipidomic analysis into HSI endmembers to demonstrate spectral changes that correlate with the specific changes of the fatty acid compositions, which are known in the literature[6,7,13]. This procedure allows to have an easily reproducible and reference model of OS for a comprehensive understanding of OS-mediated membrane alterations through biophotonic measurements. Given the established link between OS and several pathologies, including Autism Spectrum Disorder (ASD)[31–35], our investigation extended the analysis of RBC membrane HSI data comparing subjects with ASD against neurotypical (NT) controls. The severe malfunction of a membrane-embedded ionic pump, previously reported in children with ASD[31], is here correlated with HSI signatures. Our work employs a deep learning algorithm to analyze extensive hyperspectral imaging (HSI) datasets[14,36], assessing by artificial intelligence (AI) tool the potential of these data for accurate clinical predictions.

This study presents evidence showing that (a) specific changes in the distribution of the hyperspectral library of healthy RBC membranes exposed to OS correlate with specific fatty acid modifications; (b) the extent of such HSI changes are similar to those observed in RBC of individuals with ASD compared to the RBC of neurotypical individuals; (c) HSI spectra hold information on the membrane organization that may reveal structural adaptations to biochemical alterations; (d) AI analysis of HSI data allows for accurate grouping of individuals with ASD. This groundbreaking approach establishes HSI, enhanced by AI, as a robust and scalable approach leveraging RBC membrane analysis to advance membrane-based diagnostics, paving the way for advancements in OS research and personalized medicine.

Methods

Blood sample collection for the OS model experiment

A fresh capillary blood sample (500 µL) was collected from nine healthy volunteers in a Vacutainer EDTA tube (Microvette® 500 K3E, Sarstedt, Numbrecht, Germany). A signed agreement exists with the Department of Immunohematology and Transfusion Medicine (Metropolitan Area of Bologna, SIMT AMBO) to receive blood samples from healthy blood donors (Ethical Committee approval, Comitato Etico Area Vasta Emilia Romagna #0083892), accompanied by a signed informed consent for research purposes.

Preparation of the blood sample and HSI analysis

This is a modification of the previously reported procedure for analyzing RBC images using hyperspectral dark-field microscopy (HDFM)[21]. Figure 1a shows the workflow of HSI analysis for untreated blood samples.

The HDFM system consisted of a CytoViva 150 dark field condenser (CytoViva, Auburn, AL) attached to an Olympus microscope (EDFM) in place of the microscope's original condenser, via a fiber optic light guide to the lamp source. A 60× oil immersion colour-corrected objective was integral to the system. A 150 W quartz-halogen light source (Dolan-Jenner DC-950, Massachusetts, USA) was used, covering the full spectral range from 400 to 2500 nm. The calibration of the measurements is performed using two commercially available standard references (NIST polystyrene standard and the White reference standard).

All blood samples were used within 5 h after withdrawal, and reference tests were run every day before the samples arrived. In all cases, no adverse events occurred during the index test or the reference standard.

For RBC image detection, a glass slide bearing a 2 µL drop of whole blood in EDTA is placed on the microscope stage. A drop of special oil is then placed on the condenser below the slide to couple the glass slide to the condenser optically. The 10× lens was used initially to obtain an overview of a broader area of the sample and to set the focus along the *z*-axis. Identifying suitable locations or regions of interest (ROI) for image acquisition that contain round, distinct, and well-illuminated cells requires careful examination to minimise cell-cell interaction effects. Additionally, the selected ROIs must, to the extent possible, be free of background noise (e.g., from nanoparticles or plasma debris). After checking these criteria, the switch to the 60× lens is made after placing a drop of oil on the slide to couple it to the objective lens optically. In this way, the refractive index of the optical apparatus (condenser-slide-lens) is approximately constant, and the image

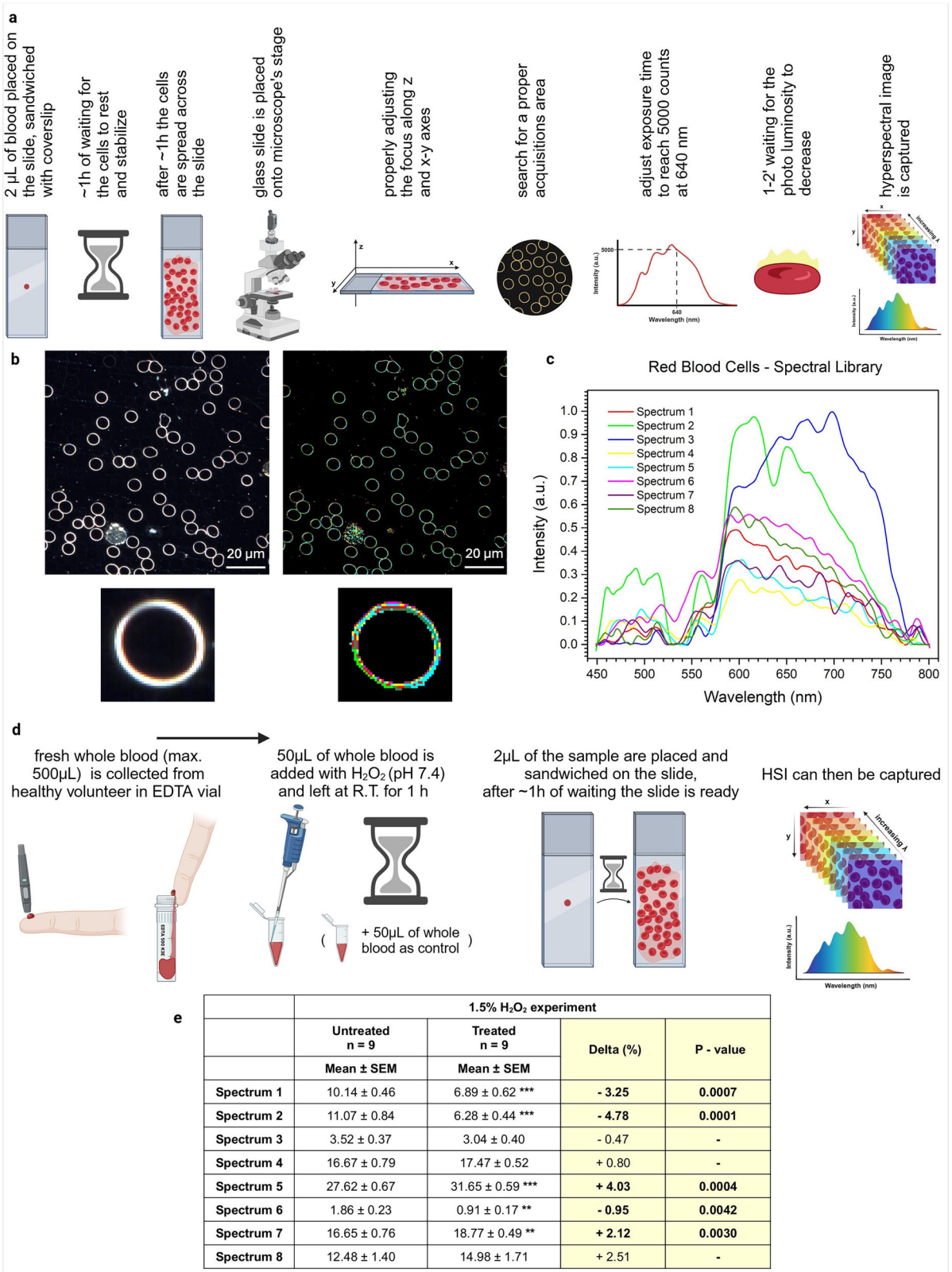

e

	1.5% H_2O_2 experiment			
	Untreated n = 9	Treated n = 9	Delta (%)	P - value
	Mean ± SEM	Mean ± SEM		
Spectrum 1	10.14 ± 0.46	6.89 ± 0.62 ***	**- 3.25**	**0.0007**
Spectrum 2	11.07 ± 0.84	6.28 ± 0.44 ***	**- 4.78**	**0.0001**
Spectrum 3	3.52 ± 0.37	3.04 ± 0.40	- 0.47	-
Spectrum 4	16.67 ± 0.79	17.47 ± 0.52	+ 0.80	-
Spectrum 5	27.62 ± 0.67	31.65 ± 0.59 ***	**+ 4.03**	**0.0004**
Spectrum 6	1.86 ± 0.23	0.91 ± 0.17 **	**- 0.95**	**0.0042**
Spectrum 7	16.65 ± 0.76	18.77 ± 0.49 **	**+ 2.12**	**0.0030**
Spectrum 8	12.48 ± 1.40	14.98 ± 1.71	+ 2.51	-

Fig. 1 | Hyperspectral image (HSI) analysis of red blood cells. Hyperspectral image (HSI) of RBC and the results of the RBC model of oxidative stress by H_2O_2: **a** Workflow of the experimental set-up for HSI detection; **b** optical field and the resulting HSI imaging with the spectral angle mapping (SAM) of a representative RBC sample, with the single cell acquisition of the eight spectral endmembers; scale bar is approximately 20 µm; **c** endmembers in the 450–800 nm range developed in this work (see Supplementary Fig. 1 in Supporting Information for details of the spectral endmembers); **d** workflow of the oxidative experiment; **e** spectral distribution of the eight endmembers in RBC of untreated and 1.5% H_2O_2 experimental models. Statistical comparisons were performed by applying unpaired two-sided *t*-test. Figure created by the authors.

is much sharper. In the Supplementary Information, further details of lamp-spectrum elimination and luminescence removal are provided (see Supplementary Fig. 3). Once the area is selected and the exposure time is set, the image is captured and displayed on the screen. Nine blood samples from healthy donors were used, yielding three RBC images from three different optical fields per sample, for a total of 81 images. The number of cells per blood sample (9 RBCs) is sufficiently large to yield low standard errors of the measurements, while remaining small enough to be handled in practice during analysis. The RBC images were collected on a range from 400 to 1000 nm (VNIR), and the Environment for Visualizing Images (ENVI, Exelis Visual Information Solutions) software version 4.4 was used for analyzing the acquired hyperspectral images and generating hyperspectral graphs. Using the Spectral Angle Mapper (SAM) algorithm, a spectral classification image was obtained, indicating the degree to which each pixel in the input image matches the endmember pixels. Subsequently, binary maps were produced to identify pixels whose similarity values exceed a predefined threshold (for more details, see SAM classification algorithm section in Supplementary Information). An optimization process was performed to establish the match between the optical and hyperspectral images. During this optimization, we used a large (up to 15) or a reduced number of endmembers to see the outcomes. Suboptimal outcomes are possible: some endmembers exhibit 0% class distribution with an under-mapping (optical image of RBC membrane partially covered) —rendering them redundant— or cause an "over-mapping" effect, where pixels outside the cell membrane (e.g., intracellular or plasma regions) are incorrectly classified (see Supplementary Fig. 1e). After the optimization, eight different hyperspectral graphs were identified, and a colour code was attributed to each of them, showing a satisfactory match with the optical images (see Fig. 1b for the images and Fig. 1c for the eight endmembers). For $n = 9$ blood samples, the percentage distributions of the eight endmembers in the healthy RBC images (81 images) were obtained and expressed as median ± standard error of the mean (SEM) in the Table shown in Fig. 1e. All analyses were performed under the conditions that prevent bias from the test performers. Experimentally, analyses were rerun to assess the extent to which the results changed. The narrow standard errors of the mean for the endmembers' distribution values indicated the method's reproducibility. The healthy RBC spectral library identified by the user and saved in ENVI is then used to map RBC in the H_2O_2-treated blood samples from the experiments described in the next section.

Blood oxidative experiment

According to the workflow in Fig. 1d, 50 µL of EDTA-treated whole blood from nine healthy volunteers was mixed with 50 µL of 1.5% or 3% (v/v) H_2O_2 in phosphate-buffered saline (PBS) at pH 7.4. The final oxidant concentrations in the mixture were 0.75% and 1.5%, respectively. The sample was left with the reagent at room temperature for 1 h, after which 2 µL were taken for HSI analysis. The remaining sample was used for membrane fatty acid analysis, as described below. Image acquisition of the nine 1.5% H_2O_2-treated blood samples yielded hyperspectral endmember distribution results shown in Fig. 1e. In Supplementary Table 2, the non-significant results for 0.75% H_2O_2 are shown.

Isolation of fatty acids from RBC membrane phospholipids and gas chromatographic analysis

The nine samples of EDTA-treated whole blood, which remained from the HSI analysis (approximately 0.4 mL), were used to perform fatty acid-based membrane lipidome analyses before and after the oxidative experiments, following a protocol described in previous studies[22]. The fatty acids are expressed in relative quantitative percentages (% rel. quant.) as mean ± SEM, and the data before and after the 1.5% H_2O_2 treatment are shown in Supplementary Table 3.

Clinical study design

The characteristics of the subjects are described in Table 1. The participant flow diagram is not shown, and the full study protocol is available, as this study utilised a subsample from a larger cohort participating in the observational study "Complexity in Autism" (presented to the Istituto delle Scienze Neurologiche, Bologna). The cohort evaluated in the present work comprises male children with idiopathic autism (ASD, $n = 27$) and neurotypically developing children (NT, $n = 31$), matched for gender, age (3 to 8 years), and BMI. Inclusion criteria for the ASD group of this study were a diagnosis based on ADOS and DSM-5 and negative results on CGH array testing. Exclusion criteria for both groups included neurological conditions, epilepsy, ongoing or recent infectious diseases (within the last 4 months), recent surgery or trauma (within the last 4 months), and intake of supplements or vitamins in the month preceding sample collection. The NT children were a consecutive series of subjects admitted to the Pediatric Surgery Ward for minimally invasive procedures, and children diagnosed with ASD enrolled at the IRCCS Istituto delle Scienze Neurologiche of Bologna, Italy. No alternative diagnoses were envisaged in the subjects without the target condition.

The observational study was conducted in accordance with the Declaration of Helsinki, and all procedures were approved by the Local Ethical Committee (Azienda USL Bologna, CE AVEC number 849-2021-OSSAUSLBO). Informed consent forms were signed by parents or legal guardians of the subjects, authorising the use of all data (including age) for research purposes. The full protocol of the observational study has been presented by the responsible clinician (Prof. Antonia Parmeggiani) at the Istituto delle Scienze Neurologiche, Bologna, with the name "Complexity in Autism". Enrolment was delayed by the COVID-19 pandemic and commenced in September 2022, with a global duration of 24 months.

In the present study, for each blood sample, the HSI procedure was performed as described above, immediately upon receipt and within 5 h of blood withdrawal, yielding nine RBC images per subject. The total number of acquisitions for NT subjects is $n = (9 \times 31) = 279$, and for ASD subjects is $n = (9 \times 27) = 243$.

Na^+/K^+-ATPase activity

ATPase activity was assayed in 1 mL of sonicated erythrocyte plasma membranes, in the presence or absence of 10 mmol/L ouabain. The blood samples analysed by this assay were the same as those analysed by HSI; only one subject in the NT group and one in the ASD group were excluded due to missing data. The inorganic phosphate (Pi) hydrolyzed from the reaction was measured in the supernatant by a colorimetric assay and normalized to the protein concentration. The procedure is detailed in a previous publication by some of us[31].

Statistics and reproducibility

Statistics were performed using GraphPad Prism 8.0 software (GraphPad Software, Inc., San Diego, CA, USA). Data were assessed for normality using the software's built-in normality tests. The following data were found to be normally distributed: HDFM spectral profiles, age and SDQ scores of two children's cohorts, and HDFM spectral and fatty acid profiles of H_2O_2-treated and untreated samples. The following data did not follow a normal distribution: BMI values for two children's cohorts and Na^+/K^+-ATPase activity values. Statistical comparisons were conducted using the parametric unpaired two-sided *t*-test or the non-parametric two-sided Mann–Whitney test, based on the normality of data distribution.

Spearman test with a 95% confidence interval was applied to assess: (i) the correlation matrix between the fatty acid profiles with HDFM spectra profiles, graphically visualized by heat maps of untreated and H_2O_2 treated samples; (ii) the correlation between the Na^+/K^+-ATPase activity and age; (iii) the correlation between the Na^+/K^+-ATPase activity and ADOS2 scores. The Linear Regression was performed between Na^+/K^+-ATPase activity values and HDFM spectra in NT and ASD subjects. Significance is given for p-value ≤ 0.05.

Artificial intelligence (AI)

This study employs advanced AI tools, primarily Supervised Artificial Neural Networks (ANNs), along with Auto-Contractive Maps (Auto-CM)

Table 1 | Clinical and demographic characteristics of the study participants

Code	Age in months	BMI	SDQ total score	Age-corrected ADOS2 score	ASD symptoms level	Code	Age in months	BMI	SDQ total score
ASD 3	62	19.22	28	8	High	NT 2	61	13.72	
ASD 4	67	17.15	43	6	Moderate	NT 4	46	15	30
ASD 5	93	15.45	37	7	Moderate	NT 5	70	12.81	33
ASD 6	66	17.08	42	10	High	NT 6	64	15.94	27
ASD 7	92	25.25	37	2	Low to Mild	NT 7	66	13.22	35
ASD 8	49	15.46	49	6	Moderate	NT 8	100	15.97	30
ASD 9	65	13.85	49	8	High	NT 9	102	24.68	28
ASD 10	41	15.61	34	9	High	NT 10	92		23
ASD 11	94	18.65	52	4	Low to Mild	NT 11	97	15.7	27
ASD 12	82	16.07	41	9	High	NT 12	61	13.89	26
ASD 13	53	18.81	60	6	Moderate	NT 13	54	13.87	38
ASD 14	46	15.35	35	4	Low to Mild	NT 14	62	15.42	35
ASD 15	87	15.98	50	8	High	NT 15	90	13.43	26
ASD 16	52	21,55	51	7	Moderate	NT 16	70	18.74	
ASD 17	104	14.7	34	6	Moderate	NT 17	42	19,53	30
ASD 18	78	14.78	41	7	Moderate	NT 18	66	14.05	37
ASD 19	78	15	35	7	Moderate	NT 19	54	17.18	46
ASD 20	50	14.88	49	8	High	NT 20	56	21.98	35
ASD 21	82	14.42	51	8	High	NT 21	97	16	33
ASD 22	83	17.36	58	8	High	NT 22	43	13.61	35
ASD 23	67	16.38	50	6	Moderate	NT 23	73	17.69	34
ASD 24	43	14.98	53	7	Moderate	NT 24	82	17.36	28
ASD 25	102	21.26		6	Moderate	NT 25	36	15	31
ASD 26	112	13.86	42	6	Moderate	NT 26	92	16.8	35
ASD 27	51	17.78	47	9	High	NT 27	73	16.53	29
ASD 28	56	16.18	49	8	High	NT 28	106	21.15	39
ASD 29	71	15.54	47	1	Low to Mild	NT 29	96	16.8	
						NT 30	72	17.04	51
						NT 31	76	17.36	
						NT 32	38	15.62	
						NT 33	98	13.22	37

ASD and NT subjects did not differ as for age and BMI. The scores of SDQ, a brief emotional and behaviour screening questionnaire for 2–17 years old patients, were significantly higher in ASD subjects (p = 1.4628E-07; pFDR: 4.3800E-07); statistical comparison were performed by applying unpaired two-sided t-test (Age and SDQ total score), and non-parametric two-sided Mann–Whitney test (BMI). *BMI* body mass index, *SDQ* strengths and difficulties questionnaire, *ADOS2* autism diagnostic observation schedule - version 2.

coupled with Minimum Spanning Tree (MST). ANNs, chosen because they are excellent at handling complex data challenges that simpler statistical models struggle with, such as:

- Dealing with outliers (extreme data points).
- Managing collinear interactions (highly correlated variables).
- Finding hidden variables or patterns.

Supervised ANNs work to learn patterns from examples related to a specific condition (like in our case, distinguishing between subjects with Autism Spectrum Disorder (ASD) and Neurotypical (NT) subjects). In the training phase, the network is fed data (inputs) and a predefined target (desired output). It computes an error function (the distance between its production and the target) and iteratively adjusts its internal parameters (weights) to minimise this error. The network's operation can be simplified as $y = f(x, w^*)$, where x is the input, y is the output, and w^* is the optimized set of parameters that best perform the prediction function f. Table 2 describes the characteristics of the ANN used in this work.

To make the predictive model as efficient as possible, with the TWIST System we eliminated the inclusion of irrelevant variables from the spectral data—those that don't help in the classification[37]. TWIST combines two powerful techniques:

- Training & Testing (T&T): A robust data re-sampling method that splits the primary dataset into multiple sub-samples (for training, testing, and validation), ensuring they all have similar statistical characteristics (probability density functions).
- Input Selective classification (IS): An evolutionary "wrapper" that actively selects the smallest number of input variables needed while still retaining all the necessary predictive information.

Both T&T and IS are driven by a powerful evolutionary computing method called the Genetic Doping Algorithm (GenD) developed at the Semeion Research centre (Rome, Italy)[37].

A critical step is optimally dividing the entire dataset into two main parts: a Training Sub-sample (A) and a Testing Sub-sample (B). The goal is to ensure that the statistical distributions of Subsets A and B are as

similar as possible. GenD's evolutionary process is used to find the perfect split. Each potential division (or "hypothesis") is represented by an "individual" in the genetic population—a vector of 1 s and 0 s indicating which records go into Sub-sample A (1) or Sub-sample B (0).

In the Fitness Evaluation (the 5-Step Check), a fitness function is used to determine whether a proposed split is good. A better split is one that generates two sub-samples (A and B) with the most similar statistical properties. This evaluation uses two independent Supervised Neural Networks (SNNs) in five steps:

Step 1: SNN_A is trained only on Subset A to learn the patterns in A.

Step 2: SNN_A is applied "blindly" to Subset B to check if what it learned from A works on B.

Step 3: SNN_B is trained only on Subset B to learn the patterns in B (independent of A).

Step 4: SNN_B is applied "blindly" to Subset A to check if what it learned from B works on A.

Step 5: The minimum of the two accuracies (from steps 2 → 4) is set as the split's fitness to ensure the split is robust and both sub-samples are statistically similar.

This "Fitness Evaluation" is repeated for every proposed split in every generation of the GenD algorithm.

In the Training and Testing Validation Protocol of the actual experiment, the dataset was made of the mean values of the nine replications of RBC images with eight inputs – the RBC endmembers - divided into two target groups: A (31 records, NT subjects) and B (27 records, ASD subjects). It was performed as follows:

1. The dataset was split into Training (A) with 31 records and Testing (B) with 27 records (Fig. 5a).
2. Run 1: ANN is trained on A and tested on B. The final weight matrix is saved.
3. Run 2: A fresh ANN is trained on B and tested on A.
4. Final Result: The results (sensitivity, specificity, and global accuracy) are expressed as the average of the two independent runs (A-B and B-A). This ensures a robust measure of the model's ability to generalize (i.e., make correct predictions on data it has never seen).

Overall results are presented as the average of the two experiments and are shown in Fig. 5a.

The auto-contractive map (Auto-CM) and minimum spanning tree (MST)

These tools are used to explore and visualize relationships within the data, rather than for prediction.

The Auto-CM identifies intricate, nonlinear relationships, clusters, and hidden patterns among variables in the dataset (see Mathematical representation and Theoretical consideration in the Supplementary Information). Therefore, the auto-contractive map function is designed to visualize the most plausible underlying interconnection schema among the variables under study. It is a unique neural network that minimizes a special cost function that includes third-order effects, allowing it to detect deeply hidden similarities. It initializes connections uniformly (making results highly reproducible) and only produces positive weights (avoiding inhibitory relationships).

The Minimum Spanning Tree (MST) simplifies and interprets the complex output matrix generated by the Auto-CM. Based on Kruskal's algorithm, it filters the Auto-CM's connections, keeping only the essential links needed to connect all variables with the minimal overall "edge weight". This creates a concise, easily interpretable graph that highlights the most critical connections in the system (a semantic connectivity map)[37–44].

Results and discussion

Non-invasive methodology to gather the scattering profiles of RBC membranes in healthy individuals, containing molecular and spatial information on protein and lipid assemblies

HSI is a strong candidate technology in non-invasive medical imaging using a readily available RBC sample[20,45], providing combined information of the molecular composition and spatial arrangement of cell components, which can be advantageously used, which enables observation of the mechanisms of stress adaptation in membrane compartments[46].

From a small volume (2 μL) of whole blood obtained from nine healthy individuals with ethylenediamine tetraacetic acid (EDTA) as the anticoagulant, RBC images in dark-field microscopy are analysed using HSI. This analysis can be performed directly on the blood sample, without any additional labelling, according to the workflow shown in Fig. 1a. EDTA is an excellent metal and, in particular a Calcium chelator[47]; beside the anticoagulant effect, it is also known to preserve the RBC samples from the Ca-dependent phospholipase enzyme activation, which leads to membrane lipid remodelling and release of polyunsaturated fatty acids-containing phospholipids[48]. The concentration of EDTA in the commercially available hematology tubes is known (1.8 mg per mL of blood). It ensures the uniformity of the chelation effect as well as of any other type of interaction of this chelator in the sample.

In applying HSI to the samples in the present work, we have introduced modifications to previously established methods to improve data quality[21,22]. In particular, we address the exposure time to achieve a maximum intensity of 5000 a.u. at 640 nm (red color for our hyperspectral imaging system), the smoothing of the original data signals using the Savitzky–Golay filtering method, and the removal of lamp spectrum and luminescence background. Details are provided in "Methods" and Supplementary Information (Supplementary Figs. 2 and 3).

Nine different EDTA-treated blood samples derived from healthy subjects are used to establish the HSI protocol. Nine RBC images are acquired from each sample, as described in the "Methods", according to the workflow depicted in Fig. 1a. Therefore, a total of $n = 81$ RBC images are obtained, representing a total number of cells evaluated per blood sample sufficiently large to yield low standard errors, while remaining small enough to be handled in practice during analysis. As described in the "Methods" for optical and hyperspectral image acquisitions, the hyperspectral library for healthy RBC was created in ENVI based on a large-scale analysis of the 81 RBC images per blood sample. The library, saved in ENVI, is used by the SAM algorithm to obtain the percent distribution of the spectral endmembers (recognized by a color code), as shown in Fig. 1b. It is worth underlining that the superimposition of the optical image with the spectral endmembers results from a very careful optimization procedure of the experimental configuration for the best HSI mapping performance, aiming at obtaining the class distribution of the endmembers with a -desired- "Gaussian-like" profile (see "Methods"). After optimization avoiding under- or over-mapping effects (see Supplementary Fig. 1e), as described in the "Methods", the HSI analysis yields eight spectral signatures (endmembers with arbitrary numbers and color codes) as reported in Fig. 1c, showing a strong scattering behaviour in the range 450–800 nm, with spectra 2 and 3 having the highest intensities. Spectrum 2 is in the blue-green region, and spectrum 3 is shifted toward the red. The other graphs are characterized by a moderate scattering efficiency at shorter wavelengths (see the list of the bands for each spectrum in Supplementary Fig. 1d). By the color codes used in the HSI detection, it is possible to appreciate the distribution of the spectral endmembers. It is worth recalling that light scattering from the RBC membrane, which is composed of clusters of molecular elements[46], encodes comprehensive information about not only the RBC's membrane composition, but also its morphology and organisation. Using the total class distributions of the endmembers (the sum of pixels across the eight signatures) as 100%, the SAM algorithm produced a class distribution report quantifying the amount of each endmember that is mapped in each RBC sample image. The results are listed in the Table of Fig. 1e (see the "Untreated" column), reported as mean ± SEM. Notably, the narrow deviations in the registered spectral endmember distribution values across the 81 images indicate limited variability and high precision in the protocol for repeated measurements. Indeed, it is gratifying to observe how homogeneous the information from the nine blood samples from different healthy individuals was. These results are obtained using blood samples kept at room temperature and analyzed within a maximum of 5 h of blood

withdrawal. Any deviation from the specified blood temperature and storage time (i.e., longer storage at room temperature or in the refrigerator at 4 °C) increased variability, thereby reducing the repeatability of the measurements. Frozen samples do not respond due to membrane alterations. In the "Methods" and Supplementary Information, the methodology is detailed, including the image acquisition procedure, the SAM classification algorithm for evaluating the spectral endmembers distribution in the RBC images, and the removal of lamp spectra and luminescence backgrounds. The analytical guide for treating the collected spectra to remove lamp spectra and luminescence is shown in Supplementary Fig. 2.

In connection with previous work, molecular components representative of the RBC membrane and sub-membrane compartments are used to examine their hyperspectral characteristics, under the same experimental conditions[21]. HSI analysis is performed on aqueous solutions or suspensions containing a single compound, such as cholesterol, phospholipids (using egg lecithin), spectrin, hemoglobin. The first two elements account for up to 50% of the membrane composition[12,46]; the latter two are associated with the sub-membrane regions and are involved in various physiopathological conditions[49]. Additionally, to examine molecular differences for oxidation by-products, two other compounds are analysed: the commercially available 7-ketocholesterol, as a representative for cholesterol oxidation, and oxyhemoglobin formed by the known reaction of hemoglobin with H_2O_2[50]. The aqueous solutions or suspensions are prepared at a molarity similar to that found in biological systems[21], as detailed in the Supporting Information. These components are characterized by scattering features, with bands in the 450–800 nm window, some of which are high-intensity (indicated with 's', sharp), as shown in Supplementary Fig. 4 and Supplementary Table 1A. The scattering data on hemoglobin and its oxidised derivative by HSI are new information, to the best of our knowledge, to combine with that reported by other methodologies. The visible absorption in the region 575–600 nm (Q bands) of hemoglobin due to the heme portion is known in the absorption spectroscopy of RBC[51]. Moreover, the bands at 542 and 577 nm are reported in the diffuse reflectance spectroscopy measurements[52], the latter being shifted to 572 nm in the HSI analysis. For hemoglobin, a sharp band at a higher wavelength (595 nm) was reported when the basic amino acids (arginine, but also histidine and lysine) display new electrostatic interactions in an acidic environment[53]. A complete understanding of the hyperspectral features of pure biomolecules and their relationship with the complexity of the membrane assembly is beyond the scope of this work and warrants further investigation in the context of hyperspectral imaging and erythrocyte analysis[20,54–56]. It is worth noting that cholesterol emerges as the most influential contributor to the RBC spectral profile in the VNIR region. It dominates the 549–694 nm range, where the most prominent peaks occur, and also appears in both the blue region (450–500 nm) and the red-IR region (675–800 nm). Interestingly, spectroscopic studies using Fourier transform infrared (FT-IR) and vibrational frequency analysis report no data for cholesterol in the visible region[57]. All data of the scattering bands for each of the studied components are shown in the Supplementary Table 1A. At the same time, Supplementary Table 1B lists the spectral bands of the eight RBC spectral endmembers in connection with those of the single compounds. Although not exhaustively describing the molecular complexity of the membrane structural components, it can be recognized that the spectral endmember 2 contains features of phospholipids (egg lecithin), cholesterol, spectrin, and does not involve hemoglobin and cholesteryl oxide. In the spectral endmember 3, spectral features of oxidized hemoglobin, cholesterol and 7-ketocholesterol are present. The spectral endmember 5 presents spectral features of hemoglobin, cholesterol, spectrin, phospholipids, and the oxidized counterparts of hemoglobin and cholesterol, with sharp bands at 554 (and 671 nm), 627, 629, 694 (and 728, 785 nm) nm. We are aware that the unmixing of a single compound cannot be achieved using such RBC membrane spectral information. Based on spectral unmixing methods, which have recently enhanced HSI for fluorescence-guided brain tumor surgery[58], further steps are needed to deepen the understanding of the individual spectral contributions arising from the complexity of the RBC membrane.

The RBCs of the healthy blood samples ($n = 9$) are then isolated and undergo work-up for the extraction of their membrane phospholipids, derivatization of all glycerol-ester-based phospholipids into their corresponding fatty acid methyl esters (FAME), according to an accredited protocol in compliance with the ISO/EIC 17025 regulation[6,7,22]. Using gas chromatographic (GC) analysis, the fatty acid composition of RBC membrane lipidome is obtained and expressed as relative quantitative percentages (mean ± SEM; see the results of untreated RBC in Supplementary Table 3). It is worth recalling that the fatty acids more sensitive to oxidative conditions are the polyunsaturated fatty acids (PUFAs), representing reliable biomarkers of such a process[1–3]. Statistical correlations are examined between the eight spectral distributions of healthy RBCs (reported in the Table of Fig. 1e) and the quantities of fatty acids in the RBC membrane lipidome of healthy individuals. In Fig. 2a, the correlation heatmap is shown (full R and p-values are reported in Supplementary Table 4). Four out of eight spectra (spectra 1, 4, 7 and 8) have distributions that correlate with the fatty acid values, whereas spectra 2, 3, 5, and 6 do not show correlations. We note that this is not an attempt to disentangle the contribution of specific fatty acids from the RBC membrane spectral features. Rather, our results suggest that HSI can characterize the membrane's overall structural organization and correlate with fatty acid composition, and we proceed to apply these findings to the OS experiment, discussed in the next section.

The oxidative treatment of blood samples determines changes in HSI spectral data and in fatty acid-based lipidomics of RBC membranes

The EDTA-collected blood samples from nine healthy volunteers are treated with hydrogen peroxide (H_2O_2) under conditions that mimic OS induced by this reagent under various physiological and pathological stressors[4,59,60]. Blood samples are examined using HSI and lipidomic analysis. Different H_2O_2 concentrations, prepared from a commercially available stock solution in phosphate-buffered saline (PBS) and titrated according to literature data[61,62], are tested for this oxidative treatment. The two concentrations of 0.75% or 1.5% H_2O_2 (as final concentrations in the samples) are chosen, after checking the absence of RBC hemolysis[63] and the non-significant increase in oxidized hemoglobin[64], which are typical indicators of severe and irreversible RBC membrane damage. The workflow of the OS experiment is shown in Fig. 1d and described in the "Experimental" section. Briefly, we incubate 50 µL of blood with an equal volume of the oxidant at the defined concentration for 1 h at room temperature; 2 µL of the mixture is used for HSI acquisition, and the remaining sample is used for RBC membrane lipidome analysis, as described above. In the optical image, no evident morphological changes are evidenced with respect to the previous healthy RBCs. From the SAM analysis of the HSI spectral graphs, the percentage distributions of the eight spectral endmembers in the RBC images are obtained (mean values ± SEM) for the 1.5% H_2O_2 experiment (Table in Fig. 1e, see column "Treated", with the reported delta (%) variations and p-values compared to the healthy "Untreated" RBC). Again, narrow deviations are observed in the repeated measurements. Five endmembers are significantly different in their distribution compared with the healthy RBCs: spectra 1, 2, 5, 6, 7, with spectra 2 and 5 showing the highest percent variations, as follows: (a) spectrum two, having an average percent distribution of 11.07 ± 0.84% in untreated samples, shows a net decrease to 6.28 ± 0.44% in the oxidized samples (delta = −4.78%; p-value = 0.0001); (b) spectrum five, with an initial value of 27.62 ± 0.67%, shows an increase in the oxidized samples up to 31.65% ± 0.59% (delta = +4.03%; $p = 0.0004$). On the other hand, when RBCs are exposed to 0.75% H_2O_2 concentration, the spectral distribution values do not significantly change compared to the untreated RBC (Supplementary Table 2).

The H_2O_2-treated blood samples are also analysed for the RBC fatty acid composition of the membrane lipidome. Statistically significant changes are found compared to the untreated RBC only for the 1.5% H_2O_2, and reported in Supplementary Table 3: the total PUFA value decreases by about 25% ($p = 0.024$), with parallel decreases in the omega-6 and omega-3 families, resulting in a ratio that remained unchanged. At the same time,

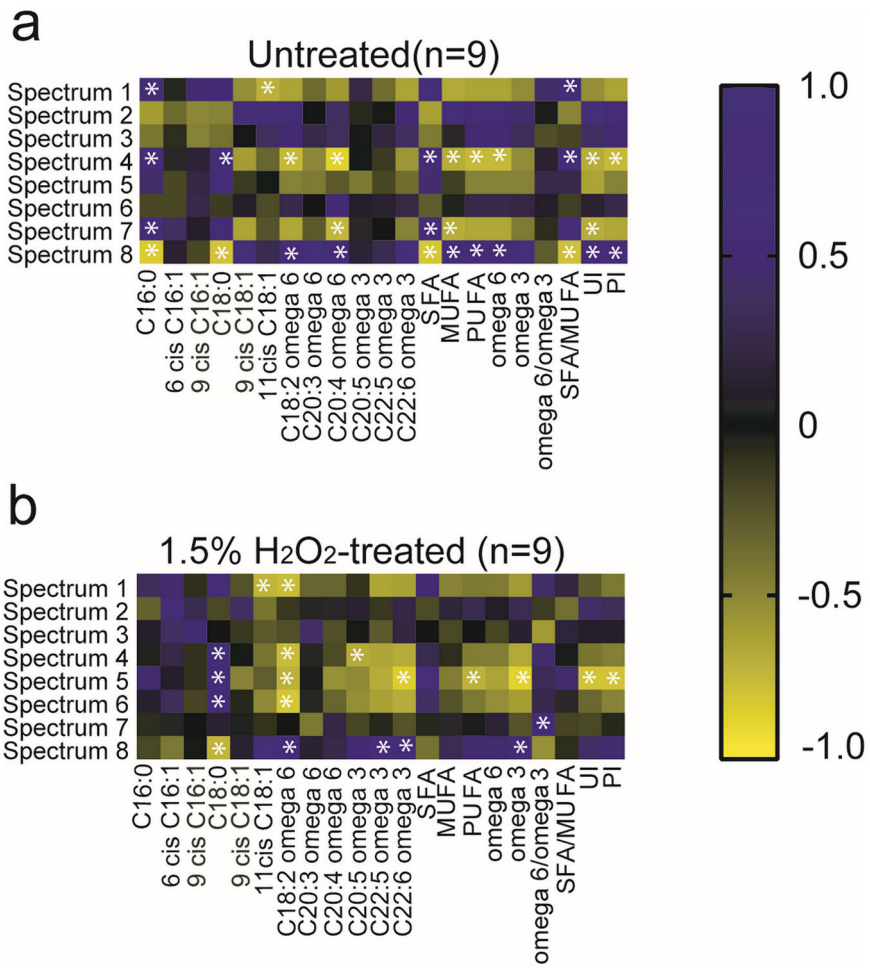

Fig. 2 | Correlations between HSI spectral endmembers and RBC membrane fatty acids before and after the oxidative insult by 1.5% H_2O_2. Correlation heatmaps of the HSI spectral distributions (values in Fig. 1e) and the RBC membrane fatty acids (values in Supplementary Table 1) for untreated (**a**) and 1.5% H_2O_2-treated RBC (**b**). Significant positive and negative correlations are indicated with asterisks, and the full correlation data are reported in Supplementary Table 4.

a

	Clinical study (Autism)			
	NT n = 31	ASD n = 27	Delta (%)	P - value
	Mean ± SEM	Mean ± SEM		
Spectrum 1	12.12 ± 0.53	7.66 ± 0.43 ***	**- 4.46**	**<0.0001**
Spectrum 2	10.72 ± 0.60	7.29 ± 0.58 ***	**- 3.43**	**0.0001**
Spectrum 3	4.17 ± 0.62	3.75 ± 0.44	- 0.42	-
Spectrum 4	19.19 ± 0.61	18.66 ± 0.55	- 0.53	-
Spectrum 5	24.98 ± 0.43	29.08 ± 0.75 ***	**+ 4.10**	**<0.0001**
Spectrum 6	4.54 ± 0.61	2.95 ± 0.69	- 1.59	-
Spectrum 7	14.75 ± 0.48	17.52 ± 0.45 ***	**+ 2.77**	**0.0001**
Spectrum 8	9.53 ± 0.97	13.08 ± 1.12 *	**+ 3.55**	**0.0190**

b

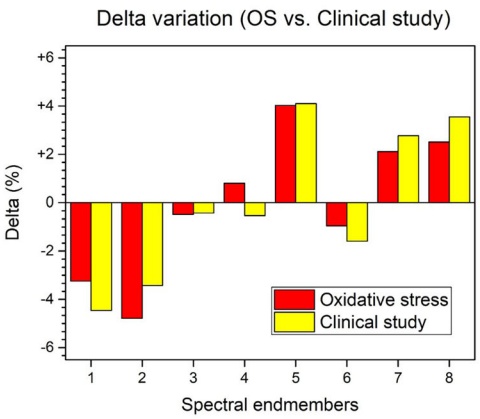

Fig. 3 | HSI data from ASD patients and NT controls and comparison with the RBC oxidative experiment. a Table of the 8 spectral endmember distributions in the HSI analysis of RBC acquired from NT ($n = 31$) and ASD ($n = 27$) children. Variations (delta) in ASD children are expressed in %, and significant p-values (≤ 0.05) are shown. Statistical comparisons were performed by applying unpaired two-sided t-test. **b** Comparison of the variations (+ or − delta %) of the 8 spectral endmembers for the H_2O_2-treated vs untreated RBC samples (OS, red bars (Fig. 1e) and for RBC samples from ASD vs NT subjects (Clinical study, yellow bars **a**). Seven out of eight RBC spectra (spectra 1,2,3.5,6,7,8) from ASD subjects and in H_2O_2-treated RBC displayed the same direction of the variations.

saturated fatty acids (SFA) increase ($p = 0.028$) by about 15%, causing a significant change in the SFA/MUFA ratio ($p = 0.04$). This compositional change results from the combined effects of PUFA peroxidation catalysed by oxidants and the exchange of damaged phospholipids with other phospholipids in the cellular pool that are rich in SFA[4,6,60]. It is worth recalling that changes in the unsaturated fatty acids of membrane phospholipids can alter the nanomechanical properties of the lipidome assembly, as evidenced by RBC PUFA rearrangements in obesity[25].

Under our experimental conditions, the blood samples contained EDTA as the anticoagulant, a known iron chelator that could reduce iron levels, as observed in several processes, including ferroptosis[65]. However, the amount of EDTA is standardised in the hematology test tube; therefore, this

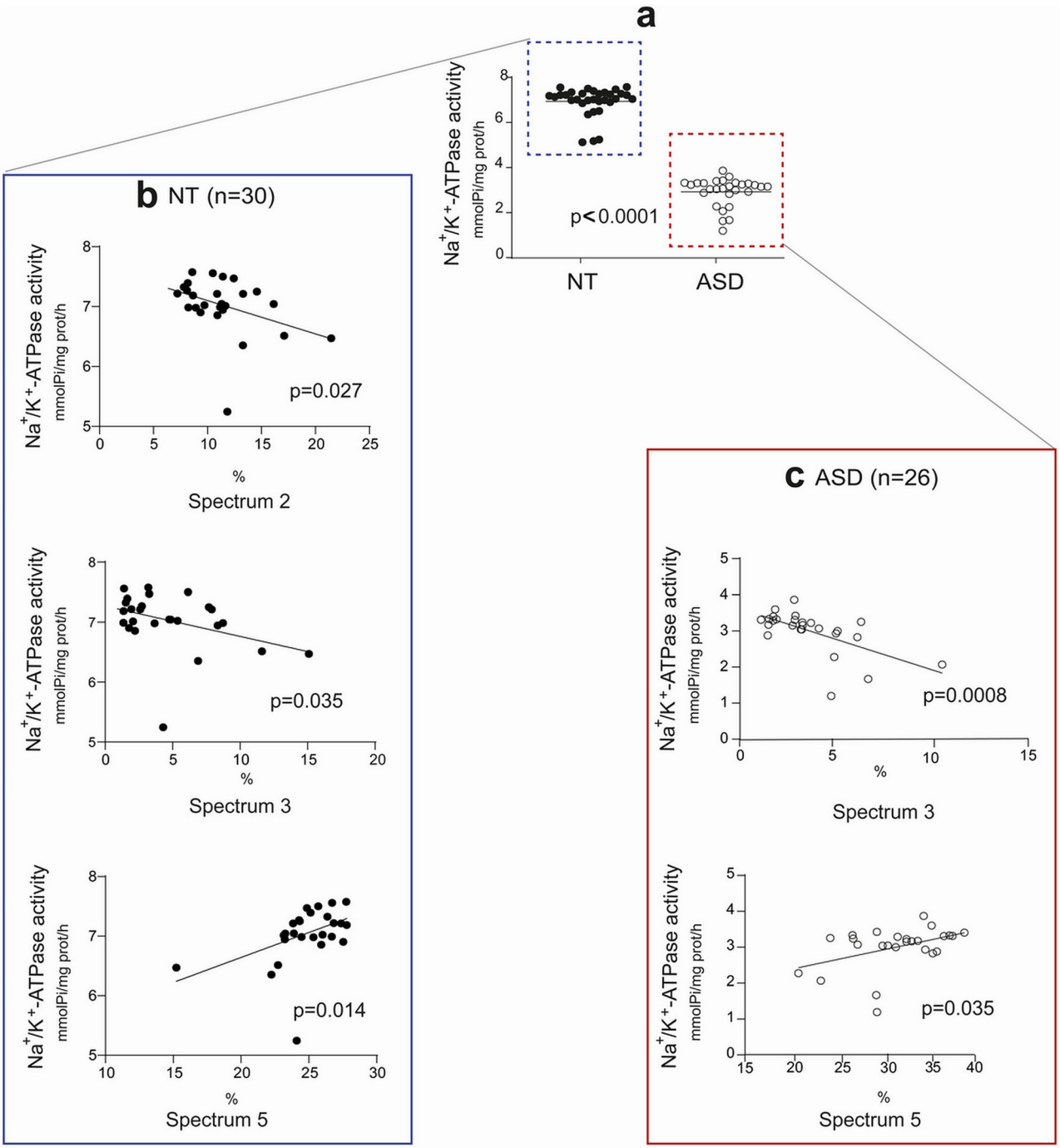

Fig. 4 | Na^+/K^+-ATPase activity and its correlations with HSI spectral distribution in RBC. a The activity of Na^+/K^+-ATPase is compared between NT ($n = 30$) and ASD ($n = 26$) children, showing a net difference between the two groups. Statistical comparison was performed by applying a non-parametric two-sided Mann–Whitney test ($p = 1.149E-34$); the significant correlations between Na^+/K^+-ATPase values and the HSI spectral endmembers distributions are shown for NT (**b**) and ASD subjects (**c**). Full data are reported in Supplementary Table 5.

effect is consistent across all samples. Other anticoagulants are not assessed at this stage, as EDTA is prioritised as an efficient calcium chelator after withdrawal, as previously explained.

Following H_2O_2 treatment and RBC isolation for membrane lipidome analysis, the correlation between the RBC membrane fatty acid composition and the percentage distribution of the eight spectral endmembers is re-evaluated. Interestingly, spectrum 5, whose distribution value increases after the OS insult, shows a different behaviour in the correlation map (Fig. 2b) compared with that reported for untreated blood samples (*cfr*, Fig. 2a; full *R* and *p*-values in Supplementary Table 4). Its distribution values now correlate with the membrane fatty acid values, showing: a positive correlation with the SFA stearic acid (C18:0, $R = +0.833$, p-value = 0.008), and negative correlations with different PUFAs, such as linoleic acid (C18:2; $R = -0.7$, p-value = 0.04), docosahexaenoic acid (C22:6, $R = -0.833$, p-value = 0.008), with total PUFA ($R = -0.700$, p-value = 0.043), total PUFA omega-3 ($R = -0.850$, p-value = 0.0006), UI (unsaturation index, $R = -0.783$, p-value = 0.017) and PI (peroxidation index, $R = -0.783$, p-value = 0.017). Overall, the increased spectral distribution of endmember 5 in HSI mapping of oxidised RBCs correlates with decreases in PUFA and an increase in SFA, suggesting that this spectral endmember primarily reflects changes in

a

ANN	Sequence	Recs	NT	ASD	Sensitivity (%)	Specificity (%)	Overall accuracy (%)	AUC	SEM
FF_Bp	AB	27	14	13	84.62	100	92.31	0.874	0.07
FF_Bp	BA	31	17	14	100	88.24	94.12	0.979	0.03
Mean					**92.31**	**94.12**	**93.21**	**0.92**	
Total		**58**	**31**	**27**					

b

	List of selected variables
1.	Spectrum_1
2.	Spectrum_2
3.	Spectrum_4
4.	Spectrum_5
5.	Spectrum_6

c

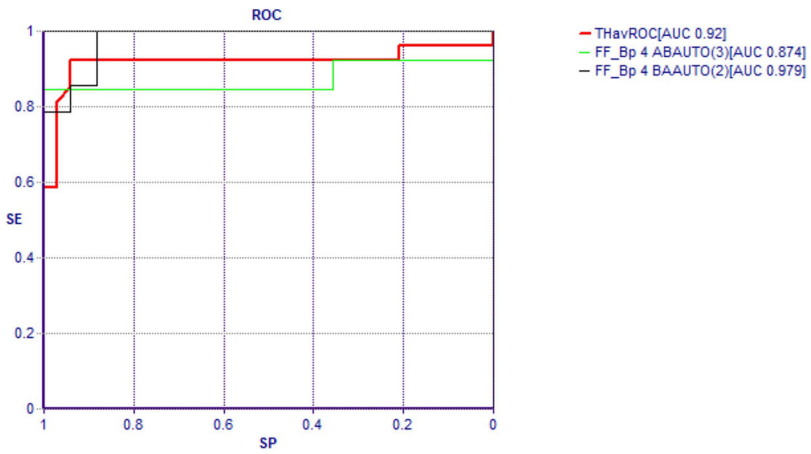

d

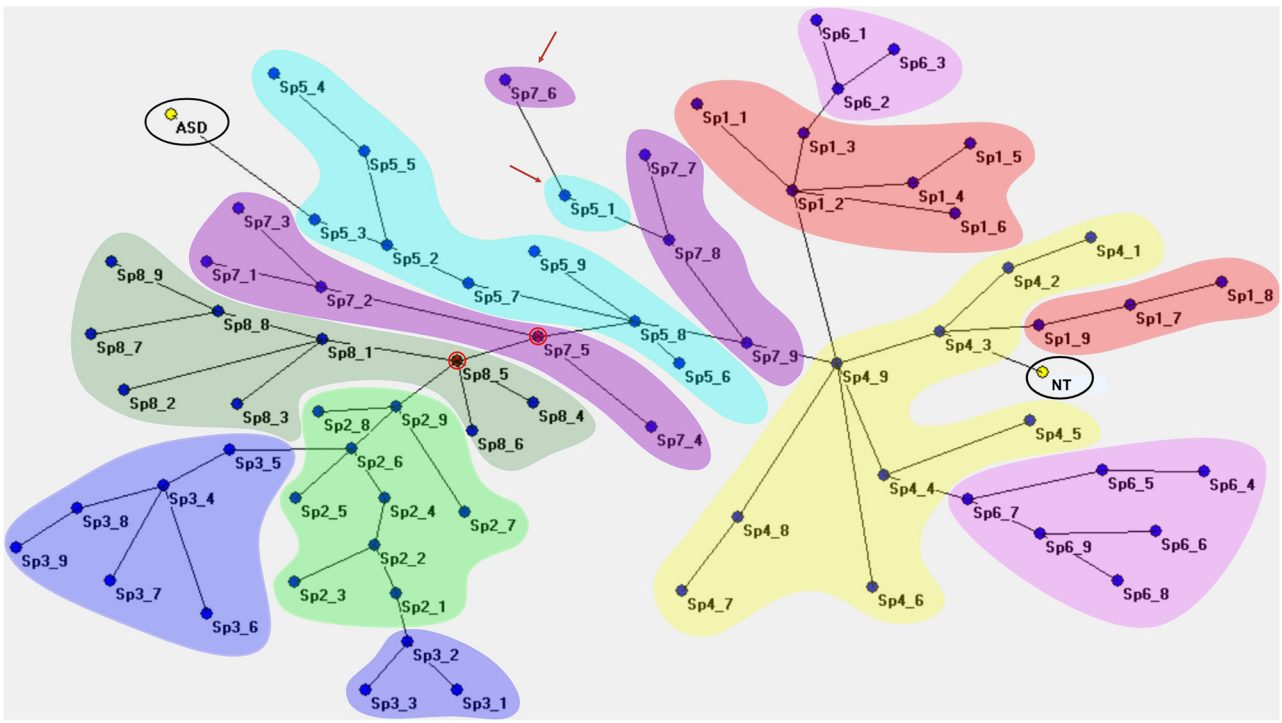

Fig. 5 | Experimental results on both experiments after TWIST and backpropagation ANN. a Results obtained with the average values of HSI spectra (8 inputs, 2 targets), by the application of backpropagation artificial neural networks with four hidden nodes to the variables selected by TWIST system, after the training-testing protocol; **b** the list of the variables selected by TWIST system; **c** the ROC curve of the experiment; **d** semantic connectivity maps generated with the combination of Auto-CM and MST algorithms.

membrane organisation induced by OS insult to the PUFA moieties. On the other hand, when considering the results with a 0,75% oxidant concentration, we can assume that this experiment serves as a "control" for the extent of perturbation, which significantly influences the membrane response. This is the first time that OS-related changes in RBC membranes have been mapped by HSI, employing a biologically relevant, well-characterised model of oxidative insult and rigorous experimental conditions. We are aware that further work, using a variety of stress insults, will improve the specificity of the endmember set, highlight the independent spectral components, and validate the use of HSI across different biological contexts.

The HSI features due to oxidative stress are also found in RBC from children with Autism Spectrum Disorder (ASD)

The OS-induced changes in RBC detected by the HSI analysis prompt us to assess whether similar spectral changes could be observed in a pathological condition involving OS. Notably, our own and others' research has identified OS markers in the blood and urine of children diagnosed with ASD conditions[31–35]. Thus, we examine RBCs from subjects with this clinical condition using HSI, compared with those from neurotypical (NT) subjects. The subjects discussed in this study are part of a larger investigation named "Complexity in Autism", collecting and evaluating a wide range of clinical, biochemical, and biological parameters in male children with idiopathic autism, and comparing these parameters with those of NT subjects, matched for sex, age (3 to 8 years of age) and BMI. Details of the sampling are given in the "Methods". Table 1 summarizes the main clinical and demographic characteristics of both cohorts.

Blood samples in EDTA of both NT ($n = 31$) and ASD ($n = 27$) groups undergo HSI analysis using the above-reported procedure (Fig. 1a). Figure 3a reports the results of the spectral distribution of the eight endmembers found for these two groups.

Five spectra show significant differences, four of them with p-values ≤ 0.0001 (spectra 1, 2, 5, 7, 8). Having the RBC model of OS as a reference for the HSI changes under an oxidative condition, we can make a comparison, evidencing a shared subset of significant spectral signatures affected in both ASD and following induction of OS (i.e., spectra 1, 2, 5, and 7; *cfr*, Figs. 1e and 3a). We focus our interest on spectra two and five of RBCs from subjects with ASD: spectrum two decreases by 3.43% ($p = 0.0001$) and spectrum five increases by 4.10% ($p < 0.0001$) compared with NT subjects. The ASD-associated spectral distribution changes of these two spectra mirror in the percent (%) and sign (+ or −) those found in the H_2O_2-treated RBCs, as shown in Fig. 3b, giving support to the hypothesis that common membrane alterations occur in the two conditions. This result provides pioneering evidence that HSI can detect changes in the components and architecture of RBC membranes, which correlate with OS-related health conditions in human subjects. It is worth emphasising that the OS model used in this work closely mimics the oxidative exposure of RBCs during blood circulation. The HSI analysis of such experimentally induced oxidative insults to RBC is linked here with a health condition known to be associated with oxidative stress. Our data points to spectrum five as the best indicator of the membrane cluster affected by OS. It must also be clarified that this result does not directly connect the use of HSI for diagnosing ASD. On the other hand, the cost-effectiveness, non-invasive nature, and broad applicability of HSI give support for extending this observational study to larger clinical settings, thereby enabling a comprehensive evaluation of its diagnostic capabilities and limitations.

Na^+/K^+-ATPase activity is severely decreased in ASD children and correlates with HSI spectral characteristics

To further investigate the relation of RBC membrane perturbation with the HSI patterns, we measure Na^+/K^+-activated Mg^{2+}-dependent ATPase activity[66] in RBC from ASD ($n = 26$) and neurotypical (NT, $n = 30$) subjects. RBCs are obtained from the same blood samples examined by HSI; one sample from the NT group and one from the ASD group are missing. Previous research demonstrated a significant decrease in this enzyme activity in individuals with ASD compared to NT[31], which is attributed to OS-related alterations in plasma membrane organization, after having rigorously excluded a wide range of other possible causes[67]. As shown in Fig. 4a (complete data in Supplementary Table 5), the RBC Na^+/K^+-ATPase activity decreases in the ASD children cohort (−57%; $p < 0.0001$), with no overlapping values between NT and ASD (NT: mean 7.053; min. 5.245; max. 7.577; ASD: mean 3.002; min. 1.197; max. 3.865). This result is an essential confirmation of previous results obtained in a different cohort of NT and ASD children[31].

Interestingly, Na^+/K^+-ATPase activity does not correlate with age-corrected ADOS-2 scores or with the subject's age (data not shown). The observed differences in Na^+/K^+-ATPase activity among the human cohorts support the involvement of oxidative stress, which is known to impair membrane protein function, as previously discussed[31,67]. The values of the Na^+/K^+-ATPase activity are correlated with the HSI spectral distributions in NT and ASD subjects, with significance for some of them (cfr, Fig. 4): spectra three and five associate with protein activity in both NT and ASD subjects, whereas the significant correlation seen for spectrum 2 in the NT subjects is lost in the ASD subjects. This finding aligns with the understanding that membrane structure and organization play crucial roles in the function of the embedded proteins, which are influenced by dynamic changes in protein-lipid interactions within the membrane[68].

Data analysis of HSI signatures with artificial intelligence Tools reveals a high sensitivity and specificity in stratifying ASD and NT subjects

Artificial Intelligence tools are used to corroborate the results of hyperspectral imaging of RBC in the stratification of NT and ASD subjects and to develop a predictive model capable of distinguishing between Autism and Typical Development conditions using the available spectral data. To evaluate the feasibility of predicting outcome (autistic vs. neurotypical) from selected variables in the study, we use supervised Artificial Neural Networks (ANNs) with a backpropagation algorithm, utilising the training and validation/test protocol developed at the Semeion Research Centre[37–44]. Figure 5a–d shows the results of ANN analysis combined with TWIST, which indicates that HSI analysis can discriminate between the two sets of subjects (NT and ASD) with high sensitivity (92.31) and specificity (94.12), overall accuracy = 93.21 and AUC = 0.92 (Fig. 5c). For details of the mathematical and technical characteristics of back propagation ANN see Table 2.

The semantic connectivity map of the variables in the study is explored by Auto-contractive map (Auto-CM), a fourth-generation artificial neural network coupled with a minimum spanning tree filter[37,38]. This tool yields the semantic connectivity map shown in Fig. 5d, where two digits identify each node. The first one refers to the spectrum (Sp) number (N.1-8), while the second refers to the spectrum replica number ($N = 1–9$). As shown, the spectrum replicas tend to cluster, except for two outliers (see arrows in Fig. 5d). The ASD group is connected to spectrum 5. In contrast, the NT group (i.e., Controls) is connected to the spectrum 4 family (variables "Controls" and "ASD" are enclosed by the black circles). Coloured areas identify replicas of the same spectral endmember. Although these results are preliminary, they suggest that spectrum 5 is the most relevant for detecting

Table 2 | Mathematical and technical characteristics of back propagation ANN*

Main ANN technical features	Main ANN architecture	
Learning law: back propagation	Input: 5	
Topology: feed forward	Hidden: 1:4	D rate: 0.1000
Temperature: Constant		W range: 1.0000
Momentum: self-momentum		Function: 4 sigmoid
Rate rule: fixed rate	Output: 2	D rate: 0.1000
Output function: soft max		W range: 1.0000
Input output: indirect connection		Function: 2 sigmoid
Input scaling: input (0,1)	Training set file: set A Training records: 31	
Target scaling: 1.000	Testing set file: set B Testing records: 27	
Number of weights: 34	Process strategy: free random	

The ANN was used to model the dataset composed of 5 variables selected by TWIST** system.
*ANN, artificial neural network; **TWIST, training with input selection and testing.

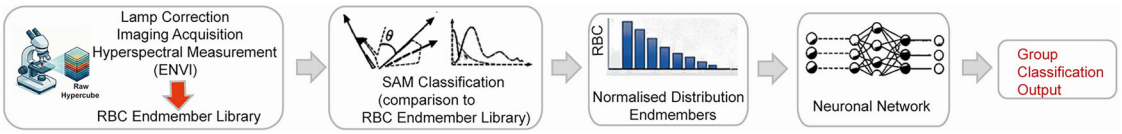

Fig. 6 | The pipeline of HSI data acquisition and AI-aided analysis. starting from a small sample of EDTA-treated whole blood, the pipeline includes: HSI acquisition and definition of the RBC endmember library collection, SAM classification with the endmember distributions in healthy and OS-related RBC, the AI-aided group classification output, recognizing OS-altered RBC. Figure created by the authors.

differences between ASD and NT individuals. These differences, which relate to a model of RBCs, appear to be associated with oxidative conditions.

In the "Methods" and Supplementary Information sections, further details of the AI protocol and AutoCM are given.

Conclusions

Figure 6 shows the entire workflow, from HSI data collection using RBC images from a small sample of EDTA-treated whole blood to the AI-based group classification of OS-affected RBC.

This study establishes a pioneering HSI protocol for identifying OS in red blood cells by utilizing a standardized OS model of H_2O_2-induced modifications as a reference against RBC from healthy donors. Specifically, this approach enables the detection of OS in children and, employing AI-driven analysis of HSI data, achieves an accuracy of 93.2% in stratifying ASD subjects. However, it is essential to underline that this methodology is not yet a diagnostic tool for identifying ASD. To fully realize its clinical potential, extensive large-scale studies are required to examine RBCs across a broader spectrum of OS-related conditions and pathologies. On the other hand, the ability of HSI to detect membrane modifications in a minimally invasive manner—requiring only two microliters of blood—and without any labeling, holds significant promise for future membrane-based diagnostics. Such a technique could guide personalized intervention aimed at promoting the natural membrane remodeling and monitoring the restoration of antioxidant protection. Notably, HSI technology provides insight into the 3-D organization of the cell membrane, an organization likely altered by OS. This explains the observed correlation between HSI features and the activity of enzymes embedded in the membrane. Ultimately, the robust and accessible nature of this HSI procedure, combined with the rapid evolution of AI, is poised to accelerate translational medical breakthroughs.

Data availability

Source data are provided with this paper as Supplementary Data file (in Excel Format).

Received: 26 March 2025; Accepted: 31 March 2026;
Published online: 14 April 2026

References

1. Forman, H. J. & Zhang, H. Targeting oxidative stress in disease: promise and limitations of antioxidant therapy. *Nat. Rev. Drug Discov.* **20**, 689–709 (2021).
2. Sies, H. Oxidative stress: concept and some practical aspects. *Antioxidants* **9**, 852 (2020).
3. Murphy, M. P. et al. Guidelines for measuring reactive oxygen species and oxidative damage in cells and in vivo. *Nat. Metab.* **4**, 651–662 (2022).
4. Orrico, F. et al. Oxidative stress in healthy and pathological red blood cells. *Biomolecules* **13**, 1262 (2023).
5. McBurney, M. I., Tintle, N. L., Vasan, R. S., Sala-Vila, A. & Harris, W. S. Using an erythrocyte fatty acid fingerprint to predict risk of all-cause mortality: the Framingham Offspring Cohort. *Am. J. Clin. Nutr.* **114**, 1447–1454 (2021).
6. Ferreri, C. & Chatgilialoglu, C. Role of fatty acid-based functional lipidomics in the development of molecular diagnostic tools. *Expert Rev. Mol. Diagn.* **12**, 767–780 (2012).
7. Ferreri, C., Sansone, A., Ferreri, R., Amézaga, J. & Tueros, I. Fatty acids and membrane lipidomics in oncology: a cross-road of nutritional, signaling and metabolic pathways. *Metabolites* **10**, 345 (2020).
8. Harris, W. S. et al. Blood n-3 fatty acid levels and total and cause-specific mortality from 17 prospective studies. *Nat. Commun.* **12**, 2329 (2021).
9. Soma, P. & Bester, J. Pathophysiological changes in erythrocytes contributing to complications of inflammation and coagulation in COVID-19. *Front. Physiol.* **13**, 899629 (2022).
10. Sherwani, S. I., Khan, H. A., Ekhzaimy, A., Masood, A. & Sakharkar, M. K. Significance of HbA1c test in diagnosis and prognosis of diabetic patients. *Biomark. Insights* **11**, 95–104 (2016).
11. Hulbert, A. J. Metabolism and longevity: is there a role for membrane fatty acids?. *Integr. Comp. Biol.* **50**, 808–817 (2010).
12. Nicolson, G. L. & Ferreira de Mattos, G. A brief introduction to some aspects of the fluid-mosaic model of cell membrane structure and its importance in membrane lipid replacement. *Membranes* **11**, 947 (2021).
13. Ferreri, C., Sansone, A., Ferocino, A., Tueros, I. & Martinez, S. A. Chapter 20 - Fatty acid profile of red blood cells as markers in dietary regimes and beyond. In *Biomarkers in Nutrition* (eds Patel, V. B., Preedy, V. R.) 1–25. https://doi.org/10.1007/978-3-030-81304-8_26-1 (Springer International Publishing, Cham, 2022).
14. Shaked, N. T., Boppart, S. A., Wang, L. V. & Popp, J. Label-free biomedical optical imaging. *Nat. Photonics* **17**, 1031–1041 (2023).
15. Barghava, A. et al. Hyperspectral imaging and its applications: a review. *Heliyon* **10**, e33208 (2024).
16. Gao, L. & Smith, R. T. Optical hyperspectral imaging in microscopy and spectroscopy – a review of data acquisition. *J. Biophoton.* **8**, 441–456 (2015).
17. Juntunen, C., Abramczyk, A. R., Woller, I. M. & Sung, Y. Hyperspectral three-dimensional absorption imaging using snapshot optical tomography. *Phys. Rev. Appl.* **18**, 034055 (2022).
18. Kurtuldu, H., Oktan, A. D., Candan, H. & Cihangiroğlu, B. S. Red blood cell analysis by hyperspectral imaging. *Nat. Appl. Sci. J.* **1**, 1–7 (2018).
19. Li, Q., Zhou, M., Liu, H., Wang, Y. & Guo, F. Red blood cell count automation using microscopic hyperspectral imaging technology. *Appl. Spectrosc.* **69**, 1372–1380 (2015).
20. Mehta, N. et al. Single-cell analysis using hyperspectral imaging modalities. *J. Biomech. Eng.* **140**, 020802 (2018).
21. Conti, M. et al. Building up spectral libraries for mapping erythrocytes by hyperspectral dark field microscopy. *Biomed. Spectrosc. Imag.* **5**, 175–184 (2016).
22. Giacometti, G. et al. High predictive values of RBC membrane-based diagnostics by biophotonics in an integrated approach for Autism Spectrum Disorders. *Sci. Rep.* **7**, 9854 (2017).
23. Park, Y. K., Best-Popescu, C. A., Dasari, R. R. & Popescu, R. Light scattering of human red blood cells during metabolic remodeling of the membrane. *J. Biomed. Opt.* **16**, 011013 (2011).
24. Park, Y. K. et al. Static and dynamic light scattering of healthy and malaria-parasite invaded red blood cells. *J. Biomed. Opt.* **15**, 020506 (2010).
25. Sot, J. et al. Erythrocyte membrane nanomechanical rigidity is decreased in obese patients. *Int. J. Mol. Sci.* **23**, 1920 (2022).

26. Kasatkin, A. & Urakov, A. Effect of hydrogen peroxide on erythrocyte temperature in vitro. *Chem. Biol. Interact.* **354**, 109837 (2022).
27. Obeagu, E. I., Igwe, M. C. & Obeagu, G. U. Oxidative stress's impact on red blood cells: Unveiling implications for health and disease. *Medicine* **103**, e37360 (2024).
28. Sies, H. Hydrogen peroxide as a central redox signaling molecule in physiological oxidative stress: oxidative eustress. *Redox Biol.* **11**, 613–619 (2017).
29. Bekeschus, S. et al. Hydrogen peroxide: a central player in physical plasma-induced oxidative stress in human blood cells. *Free Radic. Res.* **48**, 542–549 (2014).
30. Tsakanova, G. et al. Two-photon microscopy imaging of oxidative stress in human living erythrocytes. *Biomed. Opt. Express* **8**, 5834–5846 (2017).
31. Ghezzo, A. et al. Oxidative stress and erythrocyte membrane alterations in children with autism: correlation with clinical features. *PLoS ONE* **8**, e66418 (2013).
32. Liu, X. et al. Oxidative stress in Autism Spectrum Disorder-current progress of mechanisms and biomarkers. *Front. Psychiatry* **13**, 813304 (2022).
33. Bjørklund, G. et al. Oxidative stress in autism spectrum disorder. *Mol. Neurobiol.* **57**, 2314–2332 (2020).
34. Al-Saei, A. N. J. M. et al. Validation of plasma protein glycation and oxidation biomarkers for the diagnosis of autism. *Mol. Psychiatry* **29**, 653–659 (2024).
35. Panisi, C. et al. Autism spectrum disorder from the womb to adulthood: suggestions for a paradigm shift. *J. Pers. Med.* **11**, 70 (2021).
36. Li, Z. et al. Exploration of oral microbiota alteration and AI-driven non-invasive hyperspectral imaging for CAD prediction. *BMC Cardiovasc. Disord.* **25**, 102 (2025).
37. Grossi, E., Stoccoro, A., Tannorella, P., Migliore, L. & Coppedè, F. Artificial neural networks link one-carbon metabolism to gene-promoter methylation in Alzheimer's disease. *J. Alzheimers Dis.* **53**, 1517–1522 (2016).
38. Buscema, M. Artificial neural networks and complex social systems. I. Theory. *Subst. Use Misuse* **33**, 1–220 (1998).
39. Buscema, M., Breda, M. & Lodwick, W. Training with input selection and testing (TWIST) algorithm: a significant advance in pattern recognition performance of machine learning. *J. Intell. Learn. Syst. Appl.* **5**, 29–38 (2013).
40. Buscema, M. et al. An optimized experimental protocol based on neuro-evolutionary algorithms: application to the classification of dyspeptic patients and to the prediction of the effectiveness of their treatment. *Artif. Intell. Med.* **34**, 279–305 (2005).
41. Narzisi, A., Muratori, F., Buscema, M., Calderoni, S. & Grossi, E. Outcome predictors in autism spectrum disorders preschoolers undergoing treatment as usual: insights from an observational study using artificial neural networks. *Neuropsychiatr. Dis. Treat.* **11**, 1587–1599 (2015).
42. Buscema, M. et al. Artificial neural networks and artificial organisms can predict Alzheimer pathology in individual patients only on the basis of cognitive and functional status. *Neuroinformatics* **2**, 399–416 (2004).
43. Kruskal, J. B. On the shortest spanning subtree of a graph and the traveling salesman problem. *Proc. Amer. Math. Soc.* **7**, 48–50 (1956).
44. Buscema, M., Grossi, E., Snowdon, D. & Antuono, P. Auto-Contractive Maps: an artificial adaptive system for data mining. An application to Alzheimer disease. *Curr. Alzheimer Res.* **5**, 481–498 (2008).
45. Calin, M. A., Parasca, S. V., Savastru, D. & Manea, D. Hyperspectral imaging in the medical field: present and future. *Appl. Spectrosc. Rev.* **49**, 435–447 (2013).
46. van Meer, G., Voelker, D. R. & Feigenson, G. W. Membrane lipids: where they are and how they behave. *Nat. Rev. Mol. Cell Biol.* **9**, 112–124 (2008).
47. Banfi, G., Salvagno, G. L. & Lippi, G. The role of ethylenediamine tetraacetic acid (EDTA) as in vitro anticoagulant for diagnostic purposes. *Clin. Chem. Lab. Med.* **45**, 565–576 (2007).
48. Murakami, M. Phospholipase A_2. In *Encyclopedia of Signaling Molecules*. (ed Choi, S.) 3988–3999. https://doi.org/10.1007/978-3-319-67199-4_97 (Springer International Publisher, Cham, 2018).
49. Leterrier, C. & Pullarkat, P. A. Mechanical role of the submembrane spectrin scaffold in red blood cells and neurons. *J. Cell Sci.* **135**, 259356 (2022).
50. Yiping, J. et al. Structural basis of peroxide-mediated changes in human hemoglobin. *J. Biol. Chem.* **282**, 4894–4907 (2007).
51. Wojdyla, M. et al. Absorption spectroscopy of single red blood cells in the presence of mechanical deformations induced by optical traps. *J. Biomed. Opt.* **17**, 097006 (2012).
52. Zonios, G., Bykowski, J. & Kollias, N. Skin melanin, hemoglobin, and light scattering properties can be quantitatively assessed in vivo using diffuse reflectance spectroscopy. *J. Invest. Dermatol.* **11**, 1452–1457 (2001).
53. Coll-Satue, C., Jansman, M. M. T. & Hosta-Rigau, L. Comparative evaluation of UV-Vis spectroscopy-based approaches for hemoglobin quantification: method selection and practical insights. *Biomolecules* **14**, 1046 (2024).
54. Lee, J. Y. et al. Absorption-based hyperspectral imaging and analysis of single erythrocytes. *IEEE J. Sel. Top. Quantum Electron.* **18**, 1130–1139 (2012).
55. Dybas, J. et al. Trends in biomedical analysis of red blood cells – Raman spectroscopy against other spectroscopic, microscopic and classical techniques. *TrAC Trends Anal. Chem.* **146**, 116481 (2022).
56. Premasiri, W. R., Lee, J. C. & Ziegler, L. D. Surface-enhanced Raman scattering of whole human blood, blood plasma, and red blood cells: cellular processes and bioanalytical sensing. *J. Phys. Chem. B* **116**, 9376–9386 (2012).
57. Gupta, U., Singh, V. K., Kumar, V. & Khajura, Y. Spectroscopic studies of cholesterol: Fourier transform infra-red and vibrational frequency analysis. *Mater. Focus* **3**, 211–217 (2014).
58. Black, D. et al. Spectral library and method for sparse unmixing of hyperspectral images in fluorescence guided resection of brain tumors. *Biomed. Opt. Express.* **15**, 4406–4424 (2024).
59. Remigante, A. et al. Antioxidant activity of quercetin in a H_2O_2-induced oxidative stress model in red blood cells: functional role of band 3 protein. *Int. J. Mol. Sci.* **23**, 10991 (2022).
60. Ferreri, C. et al. Plasmalogens: free radical reactivity and identification of trans isomers relevant to biological membranes. *Biomolecules* **13**, 730 (2023).
61. Klassen, N. V., Marchington, D. & McGowan, H. C. E. H_2O_2 Determination by the I_3-method and by $KMnO_4$ titration. *Anal. Chem.* **66**, 2921–2925 (1994).
62. Huckaba, C. E. & Keyes, F. G. The accuracy of estimation of hydrogen peroxide by potassium permanganate titration. *J. Am. Chem. Soc.* **70**, 1640–1644 (1948).
63. Włodek, L. & Kusior, D. Oxidative hemolysis of erythrocytes. *Biochem. Mol. Biol. Educ.* **34**, 438–443 (2006).
64. Rifkind, J. M., Nagababu, E., Ramasamy, S. & Ravi, L. B. Hemoglobin redox reactions and oxidative stress. *Redox Rep.* **8**, 234–237 (2003).
65. Chen, X., Yu, C., Kang, R. & Tang, D. Iron metabolism in ferroptosis. *Front. Cell Dev. Biol.* **8**, 590226 (2020).
66. Kitao, T. & Hattori, K. Inhibition of erythrocyte ATPase activity by aclacinomycin and reverse effects of ascorbate on ATPase activity. *Experientia* **39**, 1362–1364 (1983).
67. Bolotta, A. et al. Na^+, K^+ -ATPase activity in children with autism spectrum disorder: Searching for the reason(s) of its decrease in blood cells. *Autism Res.* **11**, 1388–1403 (2018).
68. Mahato, D. R. & Andersson, M. Dynamic lipid interactions in the plasma membrane Na^+, K^+-ATPase. *Biochim. Biophys. Acta Mol. Cell. Res.* **1870**, 119545 (2023).

Acknowledgements
The authors acknowledge the generosity of the fatty acid-based membrane lipidome analyses from Lipinutragen srl. RV acknowledges Cytoviva for the financial support of his fellowship at the CNR, Bologna. The authors thank Sam Lawrence and Byron Cheatham for the loan of the HSI technology given to CF and for their technical support. The authors declare that Lipinutragen and Cytoviva had no role in the design and conduct of the study; collection, management, analysis, and interpretation of the data; preparation, review, or approval of the manuscript, and decision to submit the manuscript for publication. Blood samples and clinical data from Neurotypical children and children with Autism Spectrum Disorder were obtained in the framework of the project "Complexity in Autism", funded by the Italian Autism Federation (FIA) (#sfidAutismo20) and Associazione Cimadori Per la Ricerca Italiana sulla sindrome di Down, l'autismo e il danno cerebrale (APRI), which are here acknowledged. The authors would like to thank Mrs. Rosetta Perrini for having excellently organized the blood sampling and the clinical investigations on the children with ASD.

Author contributions
All authors confirm that they had full access to all the data in the study and accept responsibility to submit it for publication. All authors read and approved the final version of the manuscript. C.F., A.S., R.V., and M.M. conceived and designed the study. R.V., P.M.A., A.S., G.B., E.G., A.P., E.S., A.V., C.C., M.L., and E.P.E. were responsible for data collection and curation. V.D.C., A.G., C.P., M.A., C.S., A.V., and G.B. were responsible for laboratory procedures and made all formal analyses. C.F., M.M., A.P., and E.P.E. were responsible for the funds used for this study. C.F., A.S., C.C., and G.B. established and supervised lipidomic methodologies; A.P., V.D.C., M.L., A.G., C.P., and M.A. established clinical methodologies; P.M.A., C.S., A.V., and MM established biochemical methodologies; R.V., E.S., E.P.E., and E.G. established imaging and artificial intelligence methodologies of this study. C.F., M.M., and C.C. supervised the various phases of the study. C.F., R.V., A.S., E.G., and M.M. wrote the original draft and revised versions, and collected contributions from all authors.

Competing interests
CF is the co-founder and Scientific Consultant of the Lipinutragen company, born as a spin-off of the National Council of Research (CNR), but declares absence of financial and non-financial competing interests. All other authors declare no financial or non-financial competing interests.

Additional information
Supplementary information The online version contains supplementary material available at https://doi.org/10.1038/s43856-026-01581-y.

Correspondence and requests for materials should be addressed to Carla Ferreri.

Peer review information *Communications Medicine* thanks Wei Zhang and the other, anonymous, reviewer(s) for their contribution to the peer review of this work. A peer review file is available.

Reprints and permissions information is available at http://www.nature.com/reprints

Publisher's note Springer Nature remains neutral with regard to jurisdictional claims in published maps and institutional affiliations.

Open Access This article is licensed under a Creative Commons Attribution-NonCommercial-NoDerivatives 4.0 International License, which permits any non-commercial use, sharing, distribution and reproduction in any medium or format, as long as you give appropriate credit to the original author(s) and the source, provide a link to the Creative Commons licence, and indicate if you modified the licensed material. You do not have permission under this licence to share adapted material derived from this article or parts of it. The images or other third party material in this article are included in the article's Creative Commons licence, unless indicated otherwise in a credit line to the material. If material is not included in the article's Creative Commons licence and your intended use is not permitted by statutory regulation or exceeds the permitted use, you will need to obtain permission directly from the copyright holder. To view a copy of this licence, visit http://creativecommons.org/licenses/by-nc-nd/4.0/.

© The Author(s) 2026